



## Analytical Electron Microscopy of Stainless Steel Weld Metal

*On cooling, Type 304L stainless steel weld metal transforms from delta ferrite to austenite by a massive transformation*

C. E. LYMAN

**ABSTRACT.** The technique of analytical electron microscopy in a Scanning Transmission Electron Microscope (STEM) fitted with an X-ray spectrometer is described. This high spatial resolution microanalysis technique is applied to duplex Type 304L stainless steel weld metal. Small inclusions in these steels may be either iron-rich or manganese-rich silicates and may contain small amounts of elements not listed in the normal chemical analysis.

Chromium depletion at the delta ferrite/austenite interface was found to be only 0.5 wt-% Cr to a spatial resolution of 30 nm. This depletion is unlikely to be the cause of pitting corrosion observed at the  $\delta/\gamma$  phase boundary. Cr and Ni composition profiles between delta ferrite regions show that Type 304L transforms on cooling from delta ferrite to austenite by a massive transformation.

### Introduction

Many austenitic stainless steels develop a duplex, austenite plus delta ferrite, microstructure after welding. The retained delta ferrite regions are typically about 1  $\mu\text{m}$  wide and form a discontinuous network in a matrix of austenite as shown in Fig. 1A. Early experience<sup>1</sup> showed that retention of 5-10 vol-% delta ferrite in the weld

bead could be used to control hot cracking of welded austenitic steels. The amount of delta ferrite retained from high temperature can be predicted from special phase diagrams<sup>2,3</sup> and measured by metallographic and magnetic measurements.<sup>4</sup> While the retained delta ferrite is associated with reduced hot cracking, this phase can be detrimental to the aqueous corrosion,<sup>5</sup> stress corrosion cracking<sup>6</sup> and pitting susceptibility<sup>7</sup> of austenitic steels.

The present work is part of an investigation<sup>8</sup> into the reasons for increased pitting of the duplex microstructure in chloride solutions vs. an entirely austenitic structure. Garner<sup>9</sup> found for duplex Type 316L stainless steel with up to 3% retained delta ferrite that pits formed in the centers of austenite dendrites where chromium was depleted several percent with respect to the nominal composition. However, for duplex 304L steel, pits form at the  $\delta/\gamma$  interface—Fig. 1B. Tomashov *et*

*al.*<sup>10</sup> suggested that this effect was the result of chromium depletion at the  $\delta/\gamma$  boundary. To test this assumption a technique for very high spatial resolution microanalysis of chromium is required.

Segregation near the  $\delta/\gamma$  boundary of 1  $\mu\text{m}$  wide delta ferrite regions is too small in extent to allow analysis by the conventional electron beam microprobe (resolution ~ 1-3  $\mu\text{m}$ ). Techniques for analysis of fracture surfaces with good depth resolution, such as Auger electron spectroscopy, are difficult to apply to austenitic steels which resist intergranular (in this case, interphase) fracture. X-ray microanalysis of thin foil specimens appears to be the best technique currently available for high spatial resolution analysis of the heavier elements in austenitic steels. For this technique, a scanning transmission electron microscope (STEM) is required to provide a small electron probe (<10nm) with sufficient current to produce an adequate X-ray signal. The work described in this paper employed a STEM fitted with an energy dispersive X-ray spectrometer (EDS) to measure X-rays from regions of a thin specimen 30nm in diameter.

This paper shows that chromium depletion at the  $\delta/\gamma$  interface is not the reason for pit initiation on this phase boundary in 304L steel. The different pitting behavior for 316L and 304L can

---

*Paper presented during the AWS 60th Annual Meeting in Detroit, Michigan, during April 2-6, 1979, at a Symposium sponsored by the Basic Research Subcommittee of the Welding Research Council.*

C. E. LYMAN is Assistant Professor, Materials Engineering Department, Rensselaer Polytechnic Institute, Troy, New York.

be related to different solidification mechanisms for these steels.<sup>11</sup> Lippold<sup>12</sup> studied the solidification of several austenitic stainless steels and concluded that, while 316L is likely to solidify with primary austenite dendrites, 304L solidifies initially as primary delta ferrite. A solid state massive transformation transforms most of the delta ferrite of near nominal composition to austenite of similar composition.<sup>12</sup> This transformation of  $\delta$  to  $\gamma$  involving only localized diffusion<sup>13</sup> is confirmed by the present work.

### Scanning Transmission Electron Microscopy

The scanning transmission electron microscope (STEM) forms an image by scanning a small (1-5 nm) electron probe across the specimen in a raster. The brightness of the display cathode ray tube is modulated by one or more signals emitted on a point-by-point basis as the probe scans the specimen. A schematic diagram of the specimen area in a STEM with various signal detection devices is shown in Fig. 2.

For STEM images, the displayed signal can be either the beam of undeviated transmitted electrons (bright-field) or the beams which were scattered by the specimen into angles greater than about  $10^{-3}$  radians (dark-field). The bright-field image may be energy filtered by an electron spectrometer to eliminate electrons which lose energy in traversing the specimen.

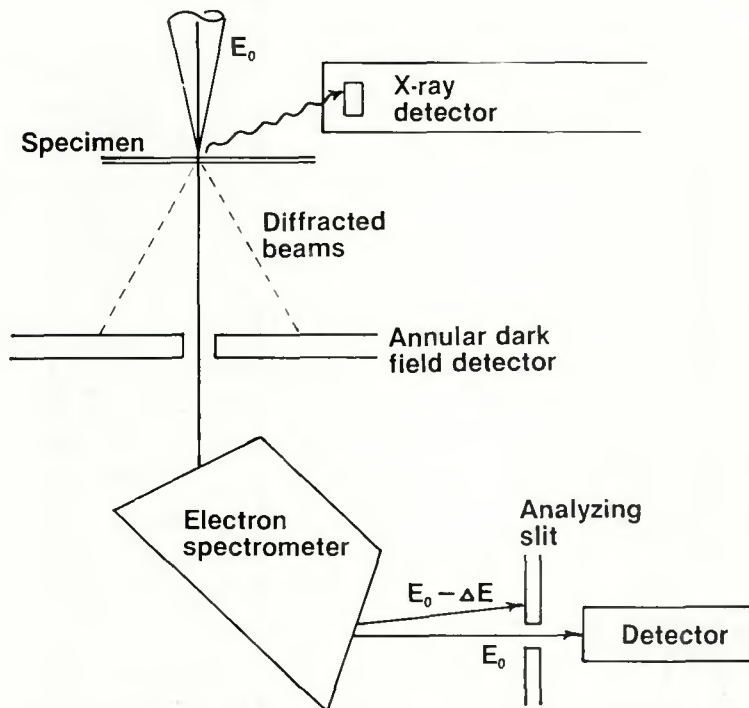


Fig. 2—Schematic diagram of components in the specimen area of an analytical scanning transmission electron microscope (STEM). Incident electrons of energy  $E_0$  generate X-rays and excite specimen atoms giving rise to characteristic energy losses  $\delta E$

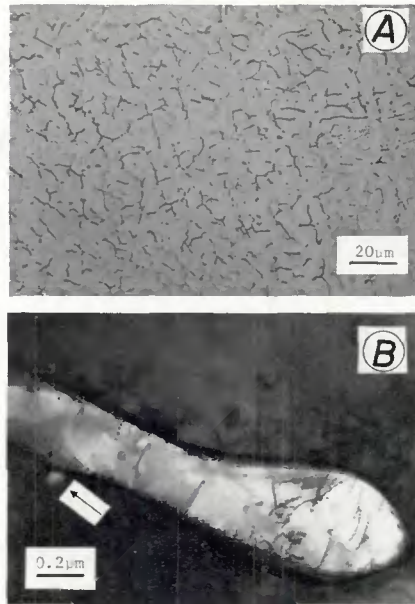


Fig. 1—Duplex stainless steel. A—reflected light micrograph of a 304L stainless steel weld showing retained delta ferrite in a matrix of austenite (Micrograph by J. C. Lippold); B—transmission electron micrograph of a delta ferrite region. Note pit (arrow) on  $\delta/\gamma$  interface formed during electropolishing of the thin foil

The same electron spectrometer can produce a characteristic electron energy loss spectrum (ELS) of electrons producing inner-shell electron ionizations. The ELS spectrum provides semi-quantitative analysis of light elements from very thin (<50 nm) speci-

mens.

The dark-field signal, collected on an annular detector, can be used to form images from much thicker regions of the specimen than the bright-field signal. This capability is useful in locating areas of the specimen to be analyzed. Backscattered electron and secondary electron images similar to those formed in a conventional surface SEM can also be displayed if suitable detectors are provided.

X-ray analysis in STEM is performed by energy dispersive spectroscopy (EDS). X-rays are detected by a semiconductor (lithium drifted silicon) detector located between the polepieces of the objective lens. Since grain boundaries and phase boundaries to be analyzed must be tilted parallel to the electron beam, the specimen should not have to be tilted toward the detector during analysis.

Care must be taken to minimize X-ray spectral backgrounds generated on internal microscope components (specimen holder, etc.) and on the specimen generally by spurious high energy X-rays or electrons. These two backgrounds can be reduced by constructing the specimen holder from light elements (Be or C) and by proper aperturing of the beam in the probe forming system, respectively.

The X-ray detector sorts X-rays by energy in addition to counting their number, and this energy spectrum (Fig. 3) is displayed on a cathode ray

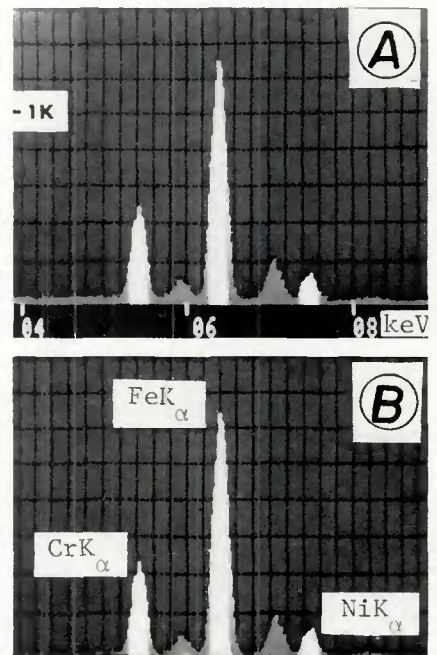


Fig. 3—Typical energy dispersive spectra (EDS) of the Type 304L stainless steel used in this work. A—before background subtraction; B—after background subtraction. Integration windows for  $CrK_{\alpha}$ ,  $FeK_{\alpha}$  and  $NiK_{\alpha}$  are lighter in contrast

tube of a multichannel analyzer. X-ray analysis must usually be performed on specimens of thickness greater than 50 nm to obtain an adequate signal. Fortunately, the range of elements detected with X-ray spectroscopy (Na to U) is the complement of that typically detected by inner-shell ionization energy loss spectroscopy (Li to Na). These two spectroscopic analyses may be obtained simultaneously.

Besides a small probe size, a STEM requires two other instrumental features for acceptable imaging and microanalysis. The probe must carry sufficient current to produce a noise-free image ( $>10^{-11}$ A) and an adequate X-ray signal ( $>10^{-9}$ A). This can only be accomplished for a probe of 5–10 nm diameter by using a high brightness electron gun. In the field emission gun used for the present work, electrons are extracted from a sharply pointed tungsten tip by a high electric field without heating.

The second important specification is the vacuum environment of the specimen. If hydrocarbon vapors (e.g., from diffusion pump oil) or other contaminants resting on the specimen are irradiated by the intense STEM electron beam, a thick carbonaceous layer builds up very rapidly and interferes with image recording and microanalysis. Thus, the pressure at the specimen must be in the ultra-high vacuum range ( $<10^{-7}$  torr  $\approx 10^{-5}$  Pa) and the specimen must be very clean.

## Experimental Procedure

### Material

The base metal for this investigation was vacuum melted 304L Type stainless steel supplied by Allegheny Ludlum Steel Corporation with the following analysis, wt-%: 18.75 Cr, 9.75 Ni, 1.55 Mn, 0.70 Si, 0.10 Cu, 0.10 Co, 0.05 Mo, 0.04 N, 0.016 S, 0.01 P, and 0.016 carbon (balance Fe).

A 23 kg (50.7 lb) cast ingot was hot and cold rolled with intermediate anneals to 0.7 mm thickness. Full penetration, autogeneous, gas tungsten arc weld beads were made according to the welding parameters shown in Table 1. Magnetic measurements showed that 6–8 vol-% of the weldment was retained delta ferrite.

### Specimen Preparation

Sections of weld metal and sections of base metal away from the weld were removed from the sheet and lapped to 125  $\mu$ m thickness. Discs were punched from the 125  $\mu$ m sheet and thinned in a dual-jet electropolishing unit using 10% perchloric acid in methanol at  $-40$  C ( $-40$  F) and 25

volts (V).

To remove surface films of elements redeposited on the surface during electropolishing, the foils were cleaned in 6kV argon ion beam for 5–10 min. Auger electron spectroscopy showed that this bombardment time was sufficient to remove chlorine and other elements left from electropolishing.

### Thin Foil Microanalysis

Thinning specimens to about 0.1  $\mu$ m substantially improves the spatial resolution of X-ray microanalysis since the 1–3  $\mu$ m deep electron diffusion zone typical of a bulk specimen is removed. For thin specimens the spatial resolution of analysis is a function of the electron probe size, specimen thickness, accelerating voltage and specimen composition. An empirical technique<sup>14</sup> can be used to convert ratios of X-ray peaks for various elements to composition, provided the specimen is thin enough to neglect the absorption and fluorescence factors of the usual microprobe correction procedure.

The thin foil specimens were analyzed in a Vacuum Generators HB5 field emission STEM fitted with an energy dispersive X-ray spectrometer. The double-tilt specimen holder was made of graphite with a slot cut in the direction of the X-ray detector. The vacuum in the specimen chamber was about  $2 \times 10^{-9}$  torr ( $2.7 \times 10^{-7}$  Pa). Electron probe spot sizes in the range 1–5 nm were adjusted to achieve at least  $10^4$  counts in the integrated  $\text{FeK}_\alpha$  peak in 30 second(s) from a 0.1  $\mu$ m thick foil. The probe current was estimated from the manufacturer's specifications to be in the range  $10^{-9}$  to  $10^{-8}$  A at 100 kV accelerating voltage.

The  $\text{CrK}_\alpha$ ,  $\text{FeK}_\alpha$ , and  $\text{NiK}_\alpha$  peaks in the X-ray spectrum were integrated by counting within the windows shown in Fig. 3. A computer-generated background, normalized to selected channels, was subtracted from the spectrum for each measurement. Ratios of X-ray peaks were converted to compositions by three equations in three unknowns based upon the Cliff-Lorimer equation:<sup>14</sup>

$$\frac{C_A}{C_B} = k_{AB} \frac{I_A}{I_B}$$

$$\frac{C_C}{C_B} = k_{CB} \frac{I_C}{I_B}$$

$$C_A + C_B + C_C + R = 1$$

where  $C_A$ ,  $C_B$ , and  $C_C$  are weight fractions of Cr, Fe, and Ni, respectively;  $I_A$ ,  $I_B$ , and  $I_C$  are background-corrected peak intensities;  $k_{AB}$  and  $k_{CB}$  are empirical constants determined from a known standard; and  $R$  is the weight fraction of the remaining alloy elements.

Table 1—Welding Parameters

Technique:	Gas tungsten arc
Electrode type:	Thoriated tungsten, centerless ground
Electrode geometry:	3.2 mm (1/8 in.) diameter, ground conical tip, 90 deg included at tip
Electrode extension:	12.7 mm (1/2 in.) from collet
Shielding gas:	High purity argon, 1.133 m <sup>3</sup> /h (40 cfh)
Welding fixture:	Copper backing and hold-down plates
Welding current:	275–300 A
Arc voltage:	12.4 V dcsp
Travel speed:	2.12 mm/s (4.98 in./h)

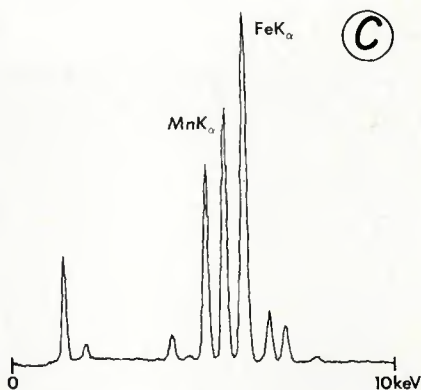
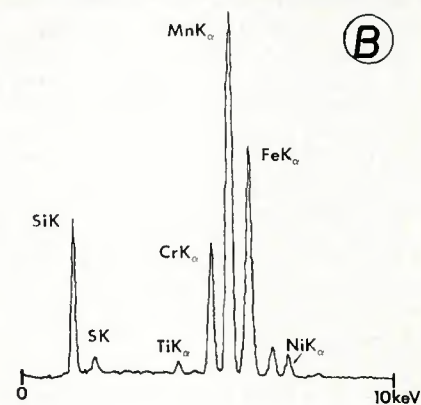
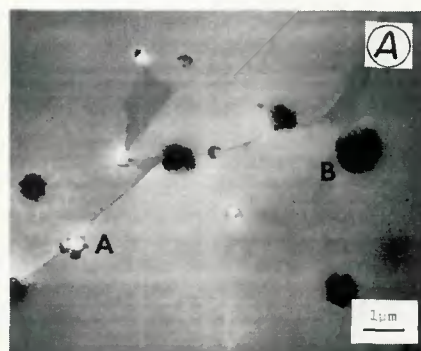


Fig. 4—Analyses of typical inclusions in Type 304L stainless steel. A—annular dark-field STEM image of inclusions near slightly darker  $\delta$ -ferrite regions; B—EDS X-ray spectrum from inclusion A; C—EDS X-ray spectrum from inclusion B

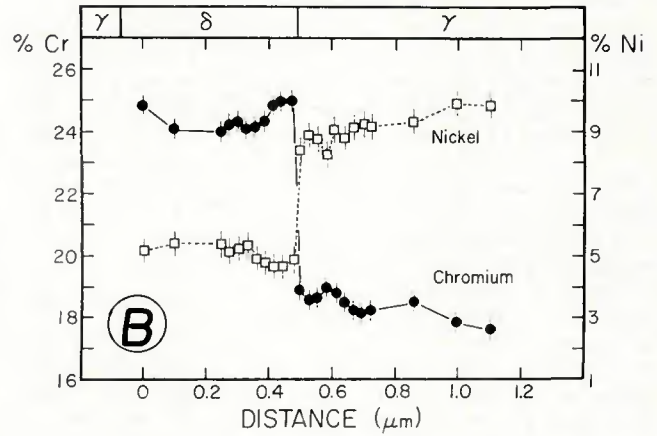
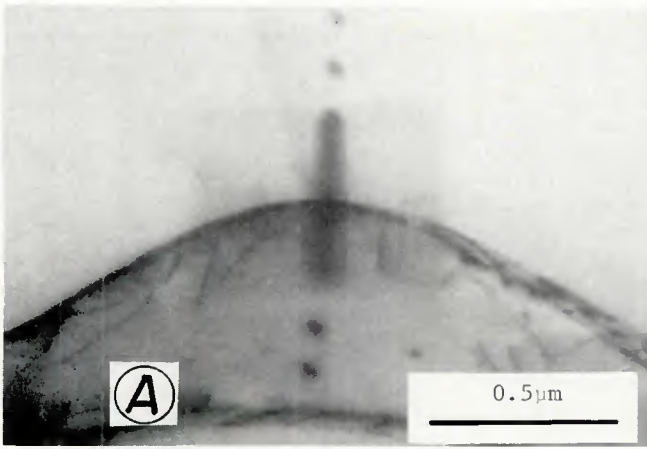


Fig. 5—Composition profile at the delta ferrite/austenite interface. A—STEM micrograph of analysis area; B—Cr and Ni concentration profiles. Foil thickness = 171 nm. (From Lyman, et al.,<sup>18</sup> courtesy Scanning Electron Microscopy)

Foils of single phase austenite base metal were used to determine the required k-values. Measured k-values should be corrected for absorption effects if analysis is in thick regions of foil. However, the absorption correction curves of Goldstein et al.<sup>15</sup> showed that no correction was required for the work reported here.

Fluorescence effects can be a problem in thin foil analysis, especially if fluorescence is predicted for a bulk specimen. For the present case, two fluorescence contributions should be noted. First, the  $FeK_{\alpha}$  line generated in the specimen can fluoresce the  $CrK_{\alpha}$  line. Lorimer<sup>16</sup> showed that the apparent increase in chromium concentration for an Fe-19Cr thin specimen is about 1 wt-% Cr. A second fluorescence problem is that due to spurious high energy X-rays or electrons bombarding the entire specimen and giving rise to detected X-rays not generated by the electron beam.<sup>17</sup> The intensity of this undesirable background varies from instrument depending on the level of shielding in the electron column.

These two fluorescence effects together may cause measurement of chromium concentrations systematically too large by a small amount. However, the results obtained were self-consistent and were corroborated, where possible, by bulk specimen microprobe data. Thus, the error bars on the measurements represent only the statistical limit of random error, i.e., the possible systematic error due to fluorescence was neglected.

Composition profiles were made by manually stepping the beam along a line perpendicular to the line between the specimen and the X-ray detector at a magnification of 200,000 times. The foil was tilted so that the phase boundary was parallel to the electron beam to maximize the spatial resolution at the boundary. The positions of the analysis points were determined from the contamination spots left by the beam during the 30 s counting time. The thickness of the foil was determined by measuring the parallax between contamination spots on the top and bottom of the foil after tilting through a known angle.

### Results

A calibration thin specimen of Type 304L stainless steel was prepared from material annealed at 1300 C (2372F) for 8 hours (h) to produce single phase austenite. Typical raw and background-subtracted X-ray spectra from austenite are shown in Fig. 3. Nine analysis points 1 μm apart across flat inclusion-free regions of austenite in two perpendicular directions were used to determine k-values and to assess the level of random error. Assuming the nominal composition for Cr and Ni, the k-values were 0.803 and 1.24 for  $k_{CrFe}$  and  $k_{NiFe}$ , respectively. The mean back-calculated chromium composition from the 18 analysis points was 18.72 wt-% with a standard deviation of  $\sigma = 0.3$  wt-%.

Figure 4 shows analyses of typical inclusions in this steel. Some inclusions appeared to be rich in manganese and others rich in iron. Silicon (presumably as a silicate), sulfur, and titanium were found in both Mn-rich and Fe-rich inclusions.

The chromium concentration profile

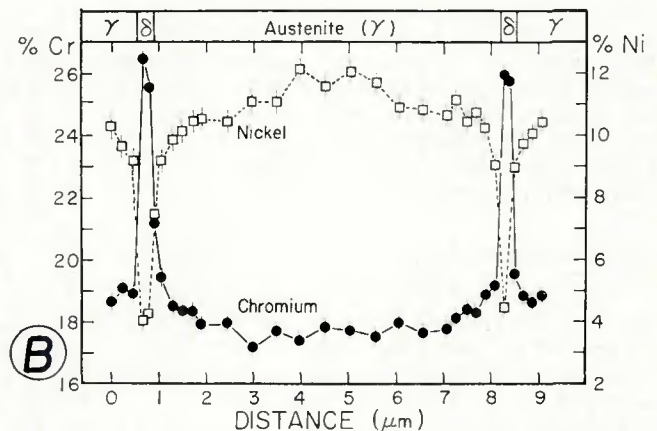


Fig. 6—STEM microanalysis between two delta ferrite regions in 304L stainless steel. A—STEM micrograph showing contamination spots at analysis points; B—Composition vs. distance profiles for Cr and Ni. (From Lyman, et al.,<sup>18</sup> courtesy Scanning Electron Microscopy)

across the delta ferrite/austenite phase boundary<sup>18</sup> is shown in Fig. 5. From the steepness of the Cr drop across the  $\delta/\gamma$  interface, the spatial resolution of analysis was estimated to be about 30 nm. Since the thickness of this area was large for this type of analysis (171 nm), better spatial resolution would be expected in thinner regions of the foil. However, very few ferrite regions were properly oriented with respect to the detector and these by chance were in rather thick areas.

Figure 6 shows composition profiles across the austenite region between two regions of ferrite. As a check on the quantitative analysis in Figs. 5 and 6, the average value of Cr in austenite and ferrite was estimated to be 18% and 25%, respectively. Assuming 7 vol-% delta ferrite overall, these values give a total Cr content of 18.56 wt-%, which is close to the nominal composition of 18.75 wt-%. A similar calculation for Ni, assuming 5 wt-% Ni in ferrite and 11 wt-% Ni in austenite, yields 10.58 wt-% Ni vs. the nominal 9.75 wt-%.

## Discussion

The composition profiles in Figs. 5 and 6 show that analytical electron microscopy can measure amounts of chromium and nickel in stainless steel with a small random error ( $\sigma = 0.3$  wt-%) and a high spatial resolution (30 nm). The small systematic errors due to fluorescence were neglected in the present work. This is reasonable since the sum of Cr contributions from each phase gives an overall composition within 1.0 wt-% of the nominal composition.

Figure 4 shows that analysis of inclusions less than 1  $\mu\text{m}$  in diameter can be made for elements heavier than sodium. Most inclusions analyzed contained Si, S, Ti, Cr, Mn, Fe and Ni. This analysis is similar to that of Astrom *et al.*<sup>19</sup> Analysis of an inclusion for elements present also in the matrix is difficult if the inclusion is actually on the underside of the foil. In that case the inclusion would appear to contain more Fe, Cr, and Ni than it actually does. A surface SEM micrograph would be useful to ascertain the location of the inclusion before analysis.

In the present case one can assume that the inclusions are both on the same side of the foil because the S peak is about the same intensity for each inclusion. This low energy X-ray line would be strongly absorbed by the FeCrNi matrix if the inclusion were located on the underside of the foil. Note that titanium was detected in both inclusions but not in the matrix.

The high resolution chromium profile of Fig. 5 shows only a 0.5 wt-% depletion of chromium within 100 nm

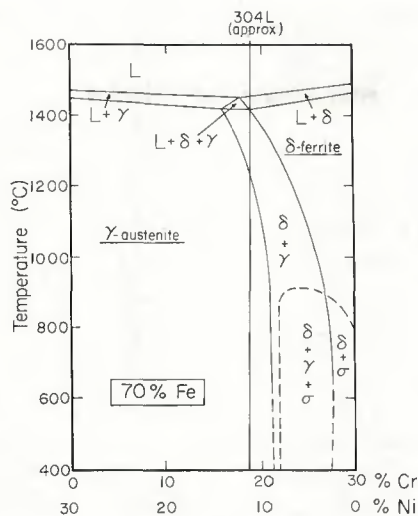


Fig. 7—70% Fe vertical section of the Fe-Cr-Ni ternary phase diagram showing the approximate composition of Type 304L stainless steel (after Masamoto, *et al.*<sup>21</sup>)

of the  $\delta/\gamma$  boundary on the austenite side. This depletion may actually be deeper and narrower than indicated with the 30 nm resolution of Fig. 5. However, if the Cr depletion is real as measured, it may arise from fast transport of atoms to the ferrite side of the phase boundary during cooling from high temperature. For this case the depletion of Cr on the austenite side of the boundary should equal the excess of Cr on the ferrite side (see Fig. 5), and it does.

The lattice diffusion coefficient for Cr in Fe at 1000 C (1832F) is  $1.4 \times 10^{-11}$   $\text{cm}^2/\text{s}$ .<sup>20</sup> This gives a diffusion distance  $2\sqrt{Dt} = 75$  nm for  $t = 1$  s. Thus, short range diffusion across the interface is a reasonable explanation for the small depletion observed. A 0.5 wt-% Cr depletion at the phase boundary is unlikely to cause pitting by itself. Some other explanation (such as phase boundary curvature or boundary segregation of impurity elements) must be sought to explain the pitting.

The difference in pit initiation site between 316L (austenite dendrite centers) and 304L ( $\delta/\gamma$  interface) can be related to the solidification mechanism for these steels. Figure 7 shows the 70% Fe vertical section<sup>21</sup> of the Fe-Cr-Ni ternary phase diagram. Lipold<sup>12</sup> showed that alloys with compositions on the low Cr side of the liquidus minimum (top of three phase triangle) solidify as primary austenite dendrites. Alloys with compositions on the high Cr side of the liquidus minimum solidify as primary delta ferrite dendrites. A different pattern of microsegregation will result depending on whether the first solid formed is austenite or ferrite.

Type 316L has a nominal composition lying within the three phase trian-

gle. Small nitrogen additions can shift the liquidus minimum to higher Cr concentrations, forcing Type 316L to solidify as primary austenite. Assuming this happened with Garner's 316L alloy,<sup>9</sup> ferrite stabilizers (e.g., Cr) would be rejected from the first austenite to solidify causing Cr depletion and pitting.

The composition of Type 304L stainless steel lies on the high Cr side of the liquidus minimum and will usually solidify as primary delta ferrite. The first ferrite to solidify will be rich in Cr and poor in Ni, the Ni being rejected into the liquid ahead of the growing dendrite. Arata *et al.*<sup>22</sup> show that 75% of the microstructure of Type 304 stainless steel is primary delta ferrite at temperatures just below the liquidus. However, at room temperature delta ferrite amounts to only 5-10% of the structure. Thus, a solid state transformation must occur to convert most of the delta ferrite to austenite.

At typical weld cooling rates, a diffusion controlled transformation mechanism is unlikely. Massalski<sup>13</sup> gives some general conditions for the nucleation and growth of a phase by a massive transformation. This type of solid-solid phase transformation occurs when two different crystal structures can be stable or metastable at the same composition but at different temperatures. This is the case for delta ferrite and austenite at the Type 304L composition—Fig. 7.

The massive transformation proceeds with no change in the overall alloy composition and with only limited diffusion confined to the interface region. This means if delta ferrite transforms to austenite massively, the concentration profile of the product austenite (Fig. 6) should show the Cr and Ni segregation patterns within the original primary delta ferrite dendrites.

To check this hypothesis Savage<sup>23</sup> used an equation derived by Smith *et al.*<sup>24</sup> to calculate the Cr profile expected for a delta ferrite dendrite growing from the liquid. The calculated profile shown in Fig. 8 corresponds both qualitatively and quantitatively to the measured profile for typical assumed growth rates and diffusion coefficients. The delta ferrite dendrite core is rich in Cr and poor in Ni since it was the first solid to freeze out. The Cr composition gradually decreases away from the dendrite center. Ni rejected during ferrite dendrite growth can be seen between the two dendrites in Fig. 6. Retained delta ferrite thus corresponds to the cores of delta ferrite dendrites with Cr contents high enough to be stable at room temperature. STEM high spatial resolution microanalysis confirms the role of the massive transformation in the

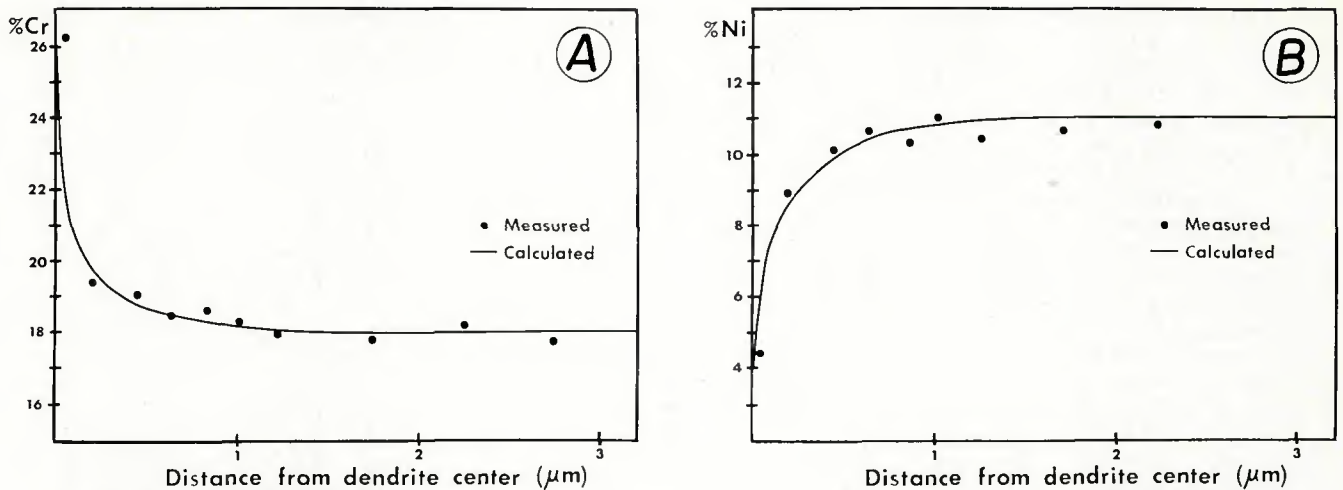


Fig. 8—Comparison of the measured Cr and Ni profiles from Fig. 6 (right side) with calculated profiles for a delta ferrite dendrite growing into liquid. A—Cr profile compared with calculation assuming the dendrite growth rate  $R = 0.21$  cm/s, Cr diffusion coefficient in liquid  $D = 5 \times 10^{-6}$  cm<sup>2</sup>/s, and the Cr equilibrium distribution coefficient  $k_0 = 1.444$ ; B—Ni profile compared with calculation assuming  $R = 0.21$  cm/s,  $D = 2 \times 10^{-6}$  cm<sup>2</sup>/s, and  $k_0 = 0.409$

formation of the duplex microstructure.

## Conclusion

Many aspects of microsegregation in Type 304L stainless steel weld metal can be analyzed by analytical electron microscopy with a STEM/X-ray spectrometer system. The spatial resolution for the technique is better than 30 nm for elements Fe, Cr, and Ni.

Some inclusions in 304L are Mn-rich, some are Fe-rich, and most have a large silicate content. Chromium depletion at the  $\delta/\gamma$  interface is small and not the cause of pits at the  $\delta/\gamma$  interface. The solid state transformation of delta ferrite to austenite in 304L weld metal takes place by a massive transformation.

## Acknowledgments

The author thanks Prof. J. B. Vander Sande for use of the Vacuum Generators HB5 field emission STEM. The author acknowledges assistance and helpful discussions from Dr. E. Hall, Dr. P. E. Manning, Dr. J. C. Lippold, Prof. D. J. Duquette, and Prof. W. F. Savage. The author is grateful for financial support from the Department of Energy under Contract No. EY-76-5-02-2462\*000.

## References

1. Scherer, R., Riedrich, G., and Hoch, G., *Arch. Eisenhut.*, **13**, 1939-1940, pp. 53-57.

2. Schaeffler, A., "Constitution Diagram of Stainless Steel Weld Metal," *Metal Progress*, **56**, 1949, pp. 680-680B.

3. Long, C., and DeLong, W., "The Ferrite Content of Austenitic Stainless Steel Weld Metal," *Welding Journal*, **52** (7), July 1973, Research Suppl., pp. 281-s to 297-s.

4. DeLong, W. T., "Ferrite in Austenitic Stainless Steel Weld Metal," *Welding Journal*, **55** (7), July 1974, Research Suppl., pp. 273-s to 286-s.

5. Gooch, T. G., "Corrosion of AISI Type 304 Austenitic Stainless Steel," *British Welding Journal*, **15**, 1968, pp. 345-357.

6. Baeslack, W. A., "A Study of Stress-corrosion Cracking in Stainless Steel Weldments Containing Ferrite," Ph.D. Thesis, Rensselaer Polytechnic Institute, 1978.

7. Odar, S. P., and Smith, H. A., Discussion, *Trans. AIME*, **135**, 1939, 526.

8. Manning, P. E., "The Effect of Environmental Variables on the Pitting Corrosion Behavior of Single and Duplex Phase 304L Stainless Steel," Ph.D. Thesis, Rensselaer Polytechnic Institute, 1978.

9. Garner, A., Presented at Corrosion/78, paper no. 20, March 6-10, 1978, National Association of Corrosion Engineers, Houston.

10. Tomashov, N. D., Chernova, C. P., Marcova, O. N., *Corrosion*, **20**, 1964, p. 166t.

11. Manning, P. E., Lyman, C. E., Savage, W. F., and Duquette, D. J., "Pit Initiation of Duplex 304L Stainless Steel in a Chloride Environment," to be published.

12. Lippold, J. C., "An Investigation of Duplex Weld Solidification in Austenitic Stainless Steels," Ph.D. Thesis, Rensselaer Polytechnic Institute, 1978.

13. Massalski, T. B., "Massive Transformations," *Materials Science and Engineering*, **25**, 1976, pp. 119-125.

14. Cliff, G., and Lorimer, G. W., "Quantitative Analysis of Thin Metal Foils Using

EMMA-4, the Ratio Technique," *Proc. 5th European Cong. on Electron Microscopy*, Manchester, Institute of Physics (London), 1972, pp. 140-141.

15. Goldstein, J. I., Costley, J. L., Lorimer, G. W., and Reed, S. J. B., "Quantitative X-ray Analysis in the Electron Microscope," *Scanning Electron Microscopy/1977*, **1**, O. Johari (ed.), Ill. Inst. Technol. Res. Inst., Chicago, pp. 315-324.

16. Lorimer, G. W., "Quantitative Analytical Electron Microscopy," *Proc. 8th Int. Conf. on X-ray Optics and Microanalysis*, Boston, 1977, paper 108.

17. Goldstein, J. I., and Williams, D. B., "Spurious X-rays Produced in the Scanning Transmission Electron Microscope," *Scanning Electron Microscopy/1978*, **1**, 1978, pp. 427-434.

18. Lyman, C. E., Manning, P. E., Duquette, D. J., and Hall, E., "STEM Microanalysis of Duplex Stainless Steel Weld Metal," *Scanning Electron Microscopy/1978*, **1**, 1978, pp. 213-220.

19. Astrom, H., Loberg, B., Bengtsson, B., and Easterling, K. E., "Hot Cracking and Microsegregation in 18-10 Stainless Steel Welds," *Metal Science*, **10**, 1976, pp. 225-234.

20. Smith, A. F., and Gibbs, G. B., "Volume and Grain-Boundary Diffusion in 20 Cr/25Ni/Nb Stainless Steel," *Metal Science Journal*, **3**, 1969, pp. 93-94.

21. Masumoto, I., Tamaki, K., and Kutsuna, M., "Hot Cracking of Austenitic Steel Weld Metal," *J. Japan Welding Soc.*, **41**, 1972, pp. 1306-1314.

22. Arata, Y., Matsuda, F., and Katayama, S., *Trans. of Japan Welding Res. Inst.*, **5**, 1976, p. 135.

23. Savage, W. F., private communication, 1978.

24. Smith, V. G., Tiller, W. A., and Rutter, J. W., *Canadian Journal of Physics*, **33**, 1955, pp. 723-745.